A Events Generation

The event stream E consists of a set of event $e = (x, y, t, p)$, where each event is triggered and recorded when the brightness change at pixel (x, y) exceeds a certain threshold C. The time interval between events is denoted as Δt_e, which is a short period, and the brightness at position $\boldsymbol{x} = (x, y)$ is represented as $F(\boldsymbol{x}, t)$. The brightness change can be calculated as $\Delta b = log(F(\boldsymbol{x}, t_e)) - log(F(\boldsymbol{x}, t_e - \Delta t_e))$. The output signal p is determined by Eq. 1.

$$p = \begin{cases} 1, & \Delta b > C \\ 0, & others \\ -1, & \Delta b < -C \end{cases} \tag{1}$$

B The Encoding Network Structure

The encoder serves as the core component of our architecture, drawing inspiration from eSL-Net [7]. However, we have made modifications to its structure by excluding the decoding segment responsible for upsampling. Consequently, we retain solely the feature extraction module, as illustrated in Fig. 8, and the code of the encoder is shown in Code (Listing. 1).

The encoder receives inputs, rolling shutter blur image I_{rsb}, and events E. The image I_{rsb} has the shape of $H \times W \times 1$ or $H \times W \times 3$, corresponding to grayscale and RGB image, respectively. Moreover, the event E is transformed into count images [9], with the shape of $H \times W \times M$, where M denotes the number of temporal divisions within the event stream. The encoder produces a high-dimensional tensor as output θ, with the shape of $H \times W \times C$.

The encoder can be decomposed into two constituent components: data preprocessing and spatio-temporal information modeling. During the preprocessing stage, the image undergoes a convolution operation to augment the channel dimensionality, while the event data is transformed into a high-dimensional Tensor using two convolutions followed by a Sigmoid activation. Subsequently, the processed tensors from the image and event data are subjected to the sparse learning module. Within the sparse learning module, both image features and event features undergo iterative cycles to derive spatio-temporal representations θ. In contrast to the original approach eSL-Net [7], we aim to incorporate deformable convolutions [8] into this loop, thereby enhancing the motion estimation and correction capabilities throughout the iterations.

C More Explanation and Discussion

Due to the constraints of the main paper's length, this supplementary section provides additional experimental details and discussions. Specifically, we elaborate on the following 11 aspects to offer readers a more comprehensive understanding of our approach:

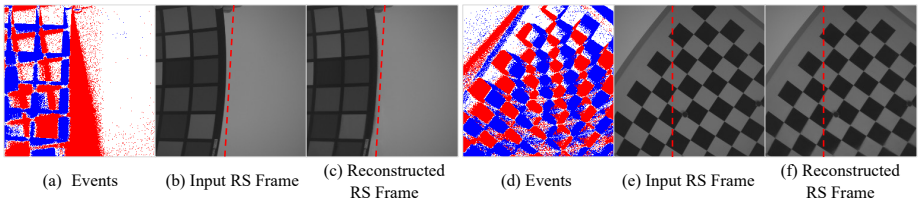

Fig. 1: Rolling shutter frame reconstruction visualization in the real-world dataset [10].

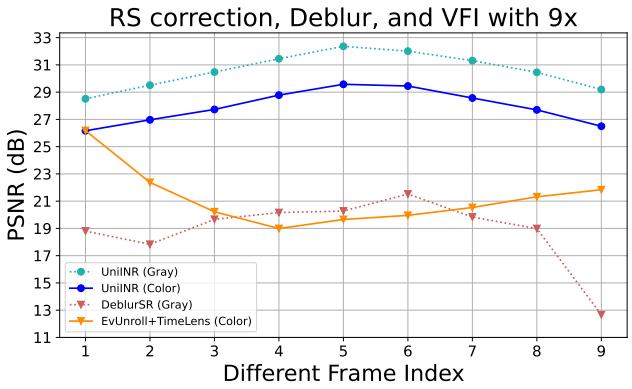

Fig. 2: The x-axis corresponds to the subscript of the frame interpolation result achieved through 9-fold frame interpolation, while the y-axis represents the PSNR value associated with each frame. A higher PSNR value indicates a higher reconstruction quality.

C.1 VFI Performance stability:

Fig. 2 illustrates the PSNR values for each frame obtained through various methods using 9-fold frame interpolation. Our proposed method demonstrates superior performance. Specifically, the intermediate image attains the highest quality, while the reconstruction quality diminishes towards both the beginning and end of the exposure, displaying a symmetrical pattern. To further enhance image quality across the entire frame, future investigations could explore the integration of multi-frame algorithms.

C.2 RS Blur Image-guided Integral Loss:

The RS blur image-guided integral Loss enhances PSNR in high interpolation settings (*e.g.*, 9×), as shown in Tab. 2. Crucially, we find our model has the generalization ability to reconstruct RS frames in the real-world dataset, as shown in Fig. 1. This underscores our method's adeptness at capturing the temporal intensity dynamics of each pixel for effective generalization in real-world.

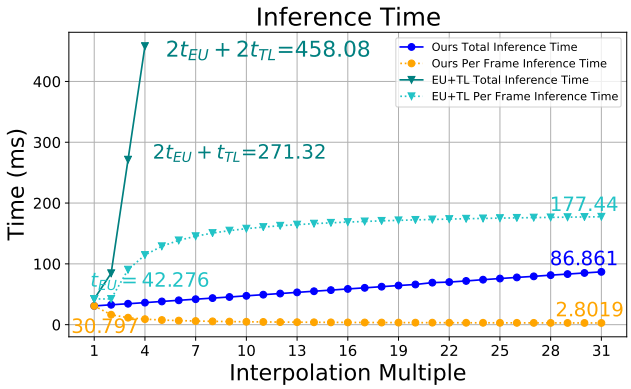

Fig. 3: Comparison of inference time of our method with EvUnroll + TimeLens. t_{EU} and t_{TL} represent the respective inference times of EvUnRoll and TimeLens. The axes represent VFI multiples (1× to 31×) and time. $2T_{EU}$ and $2t_{TL}$ means calling EvUnRoll twice and TimeLens twice.

Table 1: Ablation for position embedding.

	Position Embedding	PSNR	SSIM
1×	Sinusoid	32.46	0.9851
	Learning	**33.12**	**0.9881**
3×	Sinusoid	30.83	0.9723
	Learning	**31.11**	**0.9738**
5×	Sinusoid	30.70	**0.9678**
	Learning	**30.84**	0.9673
9×	Sinusoid	30.51	0.9560
	Learning	**30.54**	**0.9579**
		+1.11	**+0.0059**

Table 2: Ablation for the loss function.

	$\mathcal{L}_b$	PSNR	SSIM
1×	✗	33.12	0.9881
	✓	33.14	0.9844
3×	✗	31.11	0.9738
	✓	31.09	0.9768
5×	✗	30.84	0.9673
	✓	30.83	0.9784
9×	✗	30.54	0.9579
	✓	30.61	0.9538
		+0.060	**+0.0063**

C.3 Further Detail on the Dataset:

1) Gev-*Orig* dataset [10] contains original videos shot by GS high-speed cameras with 1280 × 720 resolution at 5700 fps. However, EvUnroll [10] primarily focuses on RS correction, and provided by EvUnroll Gev-RS dataset does not include RS frames with severe motion blur. Therefore, we reconstruct RS frames with severe motion blur and events from original videos. We initially downsample the original videos to DAVIS346 event camera's resolution (260 × 346) [4]. Then, we employ the event simulator vid2e [2] to synthesize events from the resized frames. We simulate RS blur frames by first generating RS sharp frames as the same RS simulation process of Fastec-RS [3] and then averaging 260 RS sharp frames after gamma correction. We use the same dataset split as EvUnroll [10], with 20 videos used for training and 9 videos used for testing. The total amounts of RS blur frames in Gev-RS [10] dataset are 784 in the training set and 441 testing set.

2) Fastec-*Orig* dataset [3] provides the original frame sequences recorded by the high-speed GS cameras with the resolution of 640 × 480 at 2400 fps. We use the same settings to resize frame sequences, create events, and RS blurry frames. Furthermore, we use the same dataset split strategy as Fastec-RS [3]: 56 sequences for training and 20 sequences for testing. Specifically, this dataset includes 1620 RS blur frames for training and 636 RS blur frames for testing.
3) Real-world dataset [10] currently the sole real dataset accessible, comprises four videos. Among these, two capture outdoor scenes, while the other two focus on indoor scenes. Each video pairs rolling shutter frames with events; the events are derived from DVS346. However, given the absence of ground truth in this dataset, it can only provide quantitative visualization results.

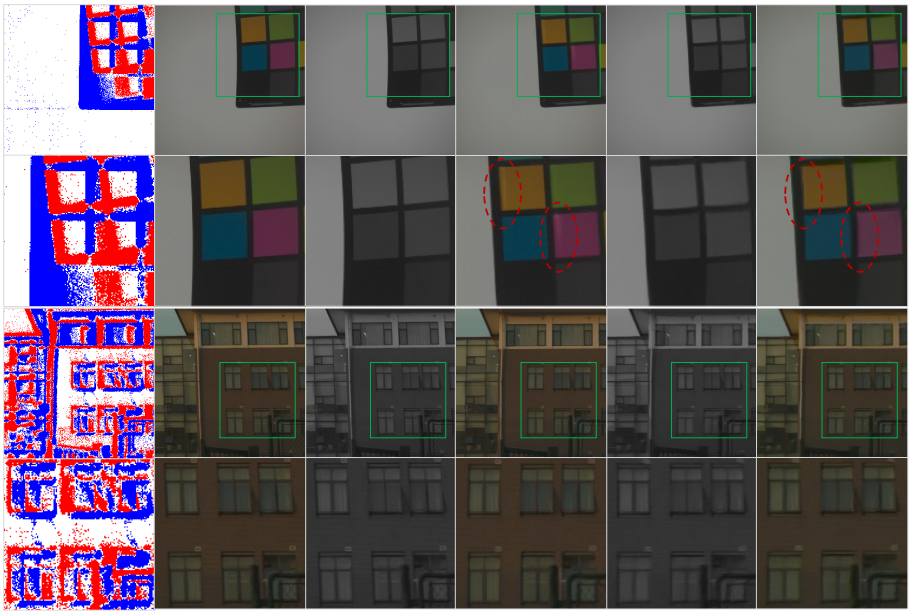

Fig. 4: Visualization results in a real-world dataset [10]. (a) is the events visualization results. (b) (c) are the input RGB and gray images that have clear rolling shutter distortions. (d) is the output of EvUnRoll. (e) (f) are the outputs of our method.

C.4 Bad case analysis:

Color distortion is due to the input's heavy blur lacking color details. Since events only record intensity (gray) changes, without color information, our method effectively outlines shapes and edges but struggles with color accuracy in this extreme example.

C.5 Extended Discussion on Inference Speed:

Fig. 3 illustrates the inference time of our method with a wide range of interpolation multiples spanning from 1× to 31×, including the total inference time and the average inference time per frame. Importantly, the total inference time increases gradually as the frame interpolation multiple increases. For instance, when going from 1× to 31× frame interpolation, the total inference time only increases from 30.8 ms to 86.9 ms. This signifies a mere 2.8-fold increase in time despite a 31-fold increase in the interpolation multiple. Additionally, it is notable that the average inference time per frame decreases with higher frame interpolation multiples. At 31× frame interpolation, the average time per frame is a mere 2.8 ms.

Our method exhibits distinct advantages over the EvUnRoll [10] and TimeLens [6] cascade approaches, particularly in terms of computational efficiency. Specifically, when the focus is solely on RS frame correction and deblurring, the inference time for EvUnRoll is measured at 42.3 ms, while our approach necessitates only 72% of that time. This computational advantage becomes even more pronounced during high-magnification frame interpolation. For instance, in scenarios requiring N-times interpolation, the cascading strategy calls for two invocations of EvUnRoll and $(N-2)$ of TimeLens, with the latter having a time cost of ($t_{TL} = 186.76\ ms$). Consequently, our method offers a significant advantage in high-magnification frame interpolation scenarios. It is crucial to note that our inference time calculations are restricted to GPU-based computations, intentionally omitting the time required for data loading and storage. In practical applications, the EvUnRoll and TimeLens cascade introduces additional disk I/O overhead, thereby further exacerbating its time consumption.

C.6 Additional Insights into the Real-World Dataset:

The visualization results for the real-world dataset can be seen in Fig. 4. The input frame, which displays a rolling shutter pattern, is characterized by clear distortions in dynamic scenes. For example, the palette's edges are curved, and the building windows tilt. In contrast, events display global shutter characteristics, as evidenced by the lack of distorted edges in the event visualizations. Both our method and EvUnRoll effectively correct the rolling shutter distortion, whether it's the distortion of the palette's edge or the deformation of building windows. However, due to the absence of ground truth, quantitative analysis remains unattainable. It's worth noting that while EvUnRoll exhibits some artifacts in the palette scenarios, our method remains artifact-free. By concurrently addressing RSC, Deblur, and VFI, our method avoids accumulating errors, leading to a more artifact-free outcome.

C.7 More Operations in Exposure Time Embedding

We perform more experiments on Gev-RS dataset [10] to validate the effect of element-wise addition, multiplication. The quantitative result is shown in Tab.

Table 3: More operation studies for exposure time embedding. (Gray blur frame as inputs in 1, 3, 5, 9 times frame interpolation).

	Time Embedding Type	PSNR	SSIM
1×	Add	*33.12*	**0.9881**
	Multiplication	**33.15**	0.9757
	Concat	**33.15**	*0.9876*
3×	Add	*31.11*	**0.9738**
	Multiplication	31.10	0.9635
	Concat	**31.14**	*0.9710*
5×	Add	30.84	**0.9673**
	Multiplication	**30.96**	*0.9684*
	Concat	*30.89*	0.9632
9×	Add	30.54	*0.9579*
	Multiplication	*30.74*	**0.9592**
	Concat	**30.77**	0.9538

3, and we find that concatenation and multiplication have higher PSNR than element-wise addition.

C.8 Analysis of PSNR and SSIM Across Different Interpolation Multiples:

In Tab. **??** of the main manuscript, we observe an intriguing discrepancy in the PSNR and SSIM metrics for 3× and 5× color frame interpolations, registering values of 28.36 and 0.9062, and 28.41 and 0.9062, respectively. Contrary to conventional wisdom, which posits that an increase in frame rate interpolation should correspondingly degrade PSNR and SSIM metrics when the model architecture remains constant, our findings deviate from this expectation. We attribute this anomaly to the network's varying predictive accuracy across the temporal spectrum. Specifically, edge frames pose a greater challenge for the network compared to those situated centrally. As illustrated in Fig. 2, for a 3× frame insertion, the terminal global shutter sharp frames contribute to 2/3 of the overall weight. Conversely, for a 5× frame insertion, the terminal frames account for only 2/5 of the weight.

C.9 Detailed Comparisons with Other Methods:

In this section, we will explain the motivations for comparing EvUnroll [10] (event-guided RS correction) in the experiment that outputs a single GS sharp frame and comparing EvUnroll + Timelens [6] (event-guided video frame interpolation) in the experiment that outputs a sequence of GS sharp frames. Fig. 7 (I) shows the process of generating a sequence of global shutter sharp (GS) frames from a rolling shutter (RS) blur image and paired events by deblur and RS correction. However, the deblur module in EvUnroll recovers the midpoint of the exposure

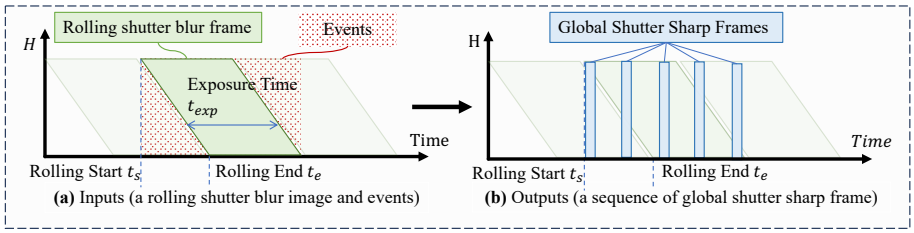

(I) Long exposure time frame as input. (Rolling shutter correction, Deblur and VFI)

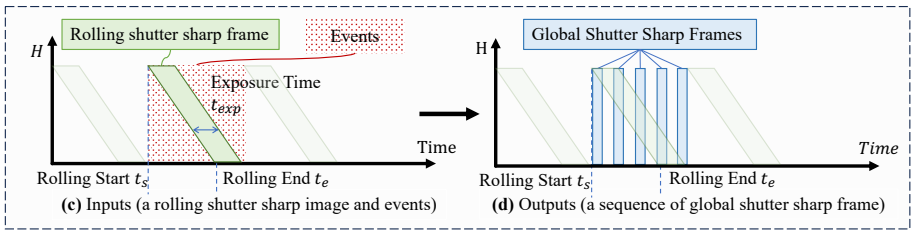

(II) Short exposure time frame as input. (Rolling shutter correction and VFI)

Fig. 5: The schematic diagram elucidates the methodologies for correcting and interpolating rolling shutter (RS) frames under varying exposure durations. Subfigure (I) delineates the procedure for long-exposure RS frames, where the presence of blur is a significant factor to be addressed. In contrast, Subfigure (II) outlines the approach for short-exposure RS frames, thereby eliminating the necessity for deblurring.

time of each row [10], as shown in Fig. 7 (b); furthermore, EvUnroll can only recover the GS sharp frames between the rolling start time t_s^m and rolling end time t_e^m of the reconstructed RS sharp frame, which can not output the arbitrary GS sharp frames during the whole exposure time of the RS blur frame. Therefore, in the joint task of deblur and RS correction, EvUnroll can not realize arbitrary frame interpolation as shown in Tab. 4 and we combine EvUnroll and Timelens in the experiment outputting a sequence of GS sharp frames. Specifically, we first generate two GS sharp frames with EvUnroll at the midpoint of the whole exposure time t_{exp} from two RS blur frames and paired events, and then we use TimeLens to generate latent GS sharp frames with the input of two GS sharp frames and events, as shown in Fig. 7 (II).

Compared with the latest research VideoINR [1], our work differs in two aspects. **a)** Different research questions: While VideoINR tackles space-time super-resolution in the global shutter by introducing implicit neural representation (INR), our proposed method first simultaneously realizes RS correction, deblurring, and frame interpolation with INR. **b)** Different methodologies: *i.* VideoINR consists of SpatialINR and TemporalINR, which are sequentially used to transfer the frame feature according to the spatial-temporal coordinate to achieve super-resolution and frame interpolation. However, SpatialINR, and TemporalINR cannot handle motion blur and rolling shutter distortion in the input frames. *ii.* In contrast, our approach develops a unified INR to simultaneously realize

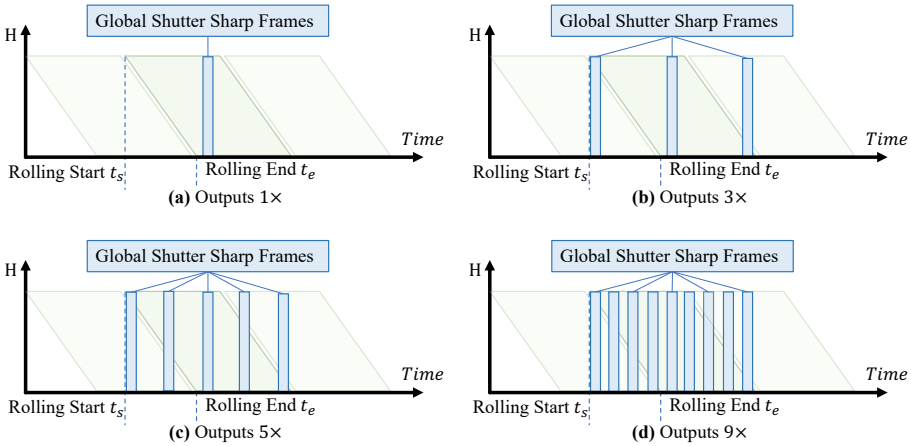

Fig. 6: Schematic diagram of frame insertion at different magnifications

Table 4: Comparison of our method with prior works.

Methods	Publication	Frames	Color	Events	Deblur	RS Correction	VFI
JCD	CVPR 2021	3	✓	✗	✓	✓	✗
eSL-Net	ECCV 2020	1	✗	✓	✓	✗	✗
eSL-Net*	ECCV 2020	1	✗	✓	✓	✓	✗
EvUnroll	CVPR 2022	1	✓	✓	✓	✓	-
TimeLens	CVPR 2021	2	✓	✓	✗	✗	✓
E-CIR	CVPR 2022	1	✗	✓	✓	✗	✓
VideoINR	CVPR 2022	2	✓	✗	✗	✗	✓
EvShutter	CVPR 2023	1	✗	✗	✓	✓	✗
DeblurSR	AAAI 2024	1	✗	✓	✓	✗	✓
NEIR	Arxiv 2023	1	✓	✓	✓	✓	✓
Ours	-	1	✓	✓	✓	✓	✓

RS correction, deblurring, and frame interpolation. Especially, according to the principle of RS and GS images, we design Exposure Time Embedding enabling the generation of RS and GS images given the specific exposure time information, which is a feat unachievable by VideoINR due to its inconsideration towards RS distortion and blur.

C.10 Visualization of Temporal Dimension Gradients:

Fig. 10 depicts the visualization of the gradients in the temporal dimension, demonstrating the successful training of the function $F(\boldsymbol{x}, t, \theta)$. Both the gradient visualization and events exhibit a similar intensity trend for $F(\boldsymbol{x}, t, \theta)$ at the specified time t. However, the gradient visualization appears smoother with more continuous edges. This observation confirms that our method is capable of learning the high temporal resolution of intensity changes present in events, simultaneously filtering out noise.

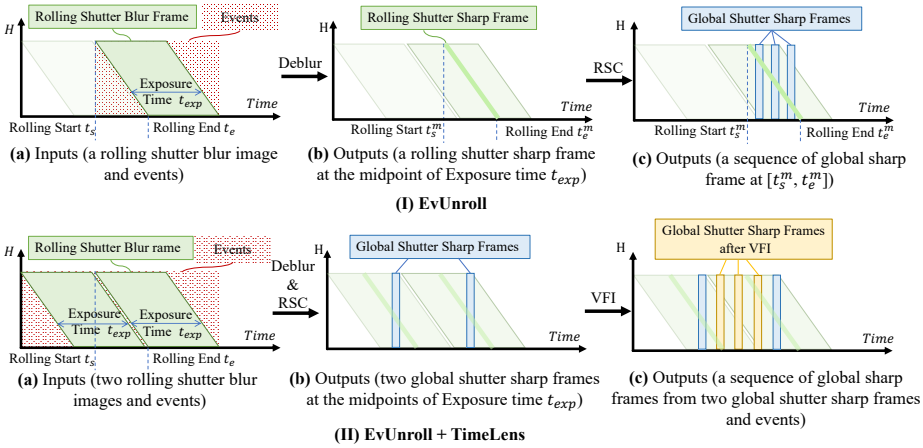

Fig. 7: Illustration of Experiment Settings of EvUnroll [10] and the combination of EvUnroll and TimeLens [6].

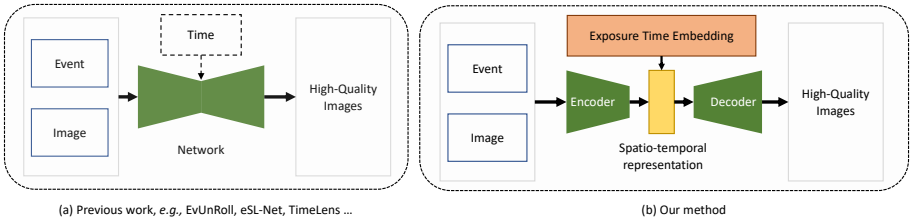

Fig. 8: Differences between our method and previous methods. In contrast to the previous method, our approach introduces spatio-temporal representation and exposure time embedding. The spatio-temporal representation involves capturing all the spatio-temporal information during the exposure time. Furthermore, specific exposure time information is embedded, which enables the decoder to generate a frame with high-quality.

C.11 Effectiveness of the DCN:

Deformable convolutions offer an effective means of modeling long-range dependencies while preserving computational efficiency. Given these advantages, we have incorporated deformable convolutions into the backbone architecture of encoding. To evaluate their impact, we conducted an ablation study, as presented in Tab. 5. Our results demonstrate an average improvement of 0.0775 dB in PSNR and 0.0088 in SSIM with the inclusion of deformable convolutions, highlighting their beneficial effect.

Due to the limited size of our dataset, we have introduced only one layer of deformable convolution. In contrast to the referenced research [8], which utilized a training set of over 14.2 million samples in the training set, our dataset is

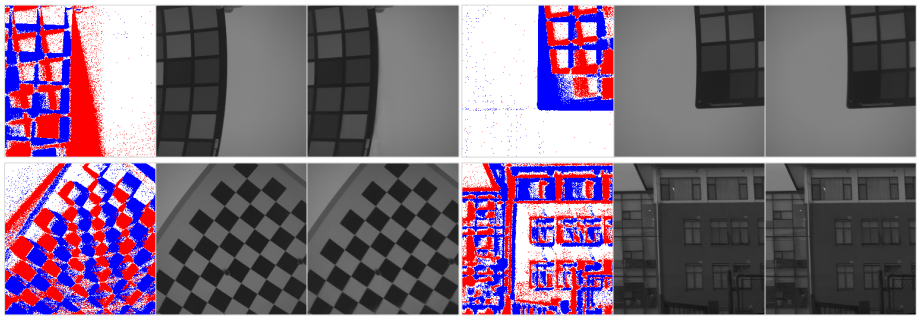

Fig. 9: Rolling shutter frame reconstruction visualization in real-world dataset.

Table 5: Ablation for deformable convolution (DC).

Interpolation multiple	DC	PSNR	SSIM
	✗	**33.15**	0.9729
1×	✓	33.12	**0.9881**
	✗	31.11	0.9701
3×	✓	**31.11**	**0.9738**
	✗	30.79	0.9609
5×	✓	**30.84**	**0.9673**
	✗	30.48	**0.9685**
9×	✓	**30.54**	0.9579
Average Increase		+ **0.0775**	+ **0.0088**

comparatively smaller. The GEV training set comprises 784 samples, while the FASTEC training set consists of 1620 samples.

C.12 Exploring Why DeblurSR Appears to Correct Rolling Shutter:

While the primary focus of the DeblurSR [5] study did not lie in the correction of the rolling shutter effect, we can observe a certain level of correction in the experiments, albeit accompanied by artifacts. We attribute this phenomenon to the fact that events themselves can be viewed as capturing a global shutter perspective. Consequently, the spiking representation learned by DeblurSR using events possesses the potential for rolling shutter correction. The effectiveness of using events to learn implicit representation for rolling shutter correction is evident.

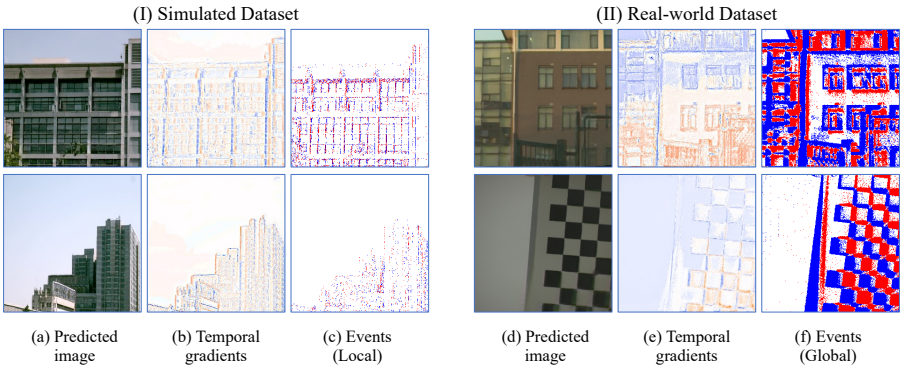

Fig. 10: (I) and (I) show visualizations on simulated and real-world datasets, respectively. From left to right: the predicted images, temporal gradients ($\partial F(\boldsymbol{x}, t, \theta)/\partial t$), and events. Orange and blue hues in the image signify positive and negative gradients, respectively. The color intensity is associated with the gradient value, with higher absolute values manifested by stronger colors.

```
import torch
import torch.nn as nn
from absl.logging import info
from egrsdb.models.unet.dcnv3_nchw import DCNv3NCHW

class _SCN(nn.Module):
    def __init__(self, hidden_channels, high_dim_channels, is_deformable, loop):
        super(_SCN, self).__init__()
        self.hidden_channels = hidden_channels
        self.high_dim_channels = high_dim_channels
        self.is_deformable = is_deformable
        self.loop = loop
        self.W1 = nn.Conv2d(hidden_channels, high_dim_channels, 3, 1, 1, bias=False)
        self.S1 = nn.Conv2d(high_dim_channels, hidden_channels, 3, 1, 1, groups=1, bias=False)
        self.S2 = nn.Conv2d(hidden_channels, high_dim_channels, 3, 1, 1, groups=1, bias=False)
        self.shlu = nn.ReLU(True)
        if is_deformable:
            self.dcn = DCNv3NCHW(channels=high_dim_channels, groups=1, offset_scale=2, act_layer="ReLU", norm_layer="LN", dw_kernel_size=3, center_feature_scale=0.25)

    def forward(self, blur_image, events):
        x1 = blur_image
        event_input = events
        x1 = torch.mul(x1, event_input)
        z = self.W1(x1)
        tmp = z
        for i in range(self.loop):
            ttmp = self.shlu(tmp)
            x = self.S1(ttmp)
            x = torch.mul(x, event_input)
            x = torch.mul(x, event_input)
            x = self.S2(x)
            if self.is_deformable:
                x = torch.relu(x)
                x = self.dcn(x)
            x = ttmp - x
            tmp = torch.add(x, z)
        c = self.shlu(tmp)
        return c
```

```
class ESLBackBone(nn.Module):
    def __init__(self, is_color, event_moments,
    hidden_channels, high_dim_channels, is_deformable, loop):
        super(ESLBackBone, self).__init__()
        in_channel = 3 if is_color else 1
        self.in_channel = in_channel
        self.event_moments = event_moments
        self.hidden_channels = hidden_channels
        self.high_dim_channels = high_dim_channels
        self.is_deformable = is_deformable
        self.loop = loop
        self.image_d = nn.Conv2d(in_channels=in_channel,
    out_channels=self.hidden_channels, kernel_size=1, stride
    =1, padding=0, bias=False)
        self.event_c1 = nn.Conv2d(in_channels=event_moments,
    out_channels=self.hidden_channels, kernel_size=1, stride
    =1, padding=0, bias=False)
        self.event_c2 = nn.Conv2d(in_channels=self.
    hidden_channels, out_channels=self.hidden_channels,
    kernel_size=1, stride=1, padding=0, bias=False)
        self.relu = nn.ReLU(inplace=True)
        self.end_conv = nn.Conv2d(in_channels=128,
    out_channels=high_dim_channels, kernel_size=3, stride=1,
    padding=1, bias=False)
        self.scn_1 = _SCN(hidden_channels, high_dim_channels,
     is_deformable, loop)

    def forward(self, events, blur_frame):
        x1 = self.image_d(blur_frame)
        event_out = self.event_c1(events)
        event_out = torch.sigmoid(event_out)
        event_out = self.event_c2(event_out)
        event_out = torch.sigmoid(event_out)
        out = self.scn_1(x1, event_out)
        out = self.end_conv(out)
        return out
```

Listing 1: The pytorch implementation of encoder.

References

1. Chen, Z., Chen, Y., Liu, J., Xu, X., Goel, V., Wang, Z., Shi, H., Wang, X.: Videoinr: Learning video implicit neural representation for continuous space-time super-resolution. In: Proceedings of the IEEE/CVF Conference on Computer Vision and Pattern Recognition. pp. 2047–2057 (2022) 7
2. Gehrig, D., Gehrig, M., Hidalgo-Carrió, J., Scaramuzza, D.: Video to events: Recycling video datasets for event cameras. In: Proceedings of the IEEE/CVF Conference on Computer Vision and Pattern Recognition. pp. 3586–3595 (2020) 3
3. Liu, P., Cui, Z., Larsson, V., Pollefeys, M.: Deep shutter unrolling network. In: Proceedings of the IEEE/CVF Conference on Computer Vision and Pattern Recognition. pp. 5941–5949 (2020) 3, 4
4. Scheerlinck, C., Rebecq, H., Stoffregen, T., Barnes, N., Mahony, R., Scaramuzza, D.: Ced: Color event camera dataset. In: Proceedings of the IEEE/CVF Conference on Computer Vision and Pattern Recognition Workshops. pp. 0–0 (2019) 3
5. Song, C., Bajaj, C., Huang, Q.: Deblursr: Event-based motion deblurring under the spiking representation. arXiv preprint arXiv:2303.08977 (2023) 10
6. Tulyakov, S., Gehrig, D., Georgoulis, S., Erbach, J., Gehrig, M., Li, Y., Scaramuzza, D.: Time lens: Event-based video frame interpolation. In: Proceedings of the IEEE/CVF conference on computer vision and pattern recognition. pp. 16155–16164 (2021) 5, 6, 9
7. Wang, B., He, J., Yu, L., Xia, G.S., Yang, W.: Event enhanced high-quality image recovery. In: Computer Vision–ECCV 2020: 16th European Conference, Glasgow, UK, August 23–28, 2020, Proceedings, Part XIII 16. pp. 155–171. Springer (2020) 1
8. Wang, W., Dai, J., Chen, Z., Huang, Z., Li, Z., Zhu, X., Hu, X., Lu, T., Lu, L., Li, H., et al.: Internimage: Exploring large-scale vision foundation models with deformable convolutions. arXiv preprint arXiv:2211.05778 (2022) 1, 9
9. Zheng, X., Liu, Y., Lu, Y., Hua, T., Pan, T., Zhang, W., Tao, D., Wang, L.: Deep learning for event-based vision: A comprehensive survey and benchmarks. arXiv preprint arXiv:2302.08890 (2023) 1
10. Zhou, X., Duan, P., Ma, Y., Shi, B.: Evunroll: Neuromorphic events based rolling shutter image correction. In: Proceedings of the IEEE/CVF Conference on Computer Vision and Pattern Recognition. pp. 17775–17784 (2022) 2, 3, 4, 5, 6, 7, 9